Article

www.the-innovation.org

Multifunctional succinate additive for flexible perovskite solar cells with more than 23% power-conversion efficiency

Minghao Li,[1] Junjie Zhou,[1] Liguo Tan,[1] Hang Li,[1] Yue Liu,[1] Chaofan Jiang,[1] Yiran Ye,[1] Liming Ding,[2] Wolfgang Tress,[3] and Chenyi Yi[1,*]

*Correspondence: yicy@tsinghua.edu.cn

Received: June 9, 2022; Accepted: August 31, 2022; Published Online: September 6, 2022; https://doi.org/10.1016/j.xinn.2022.100310

GRAPHICAL ABSTRACT

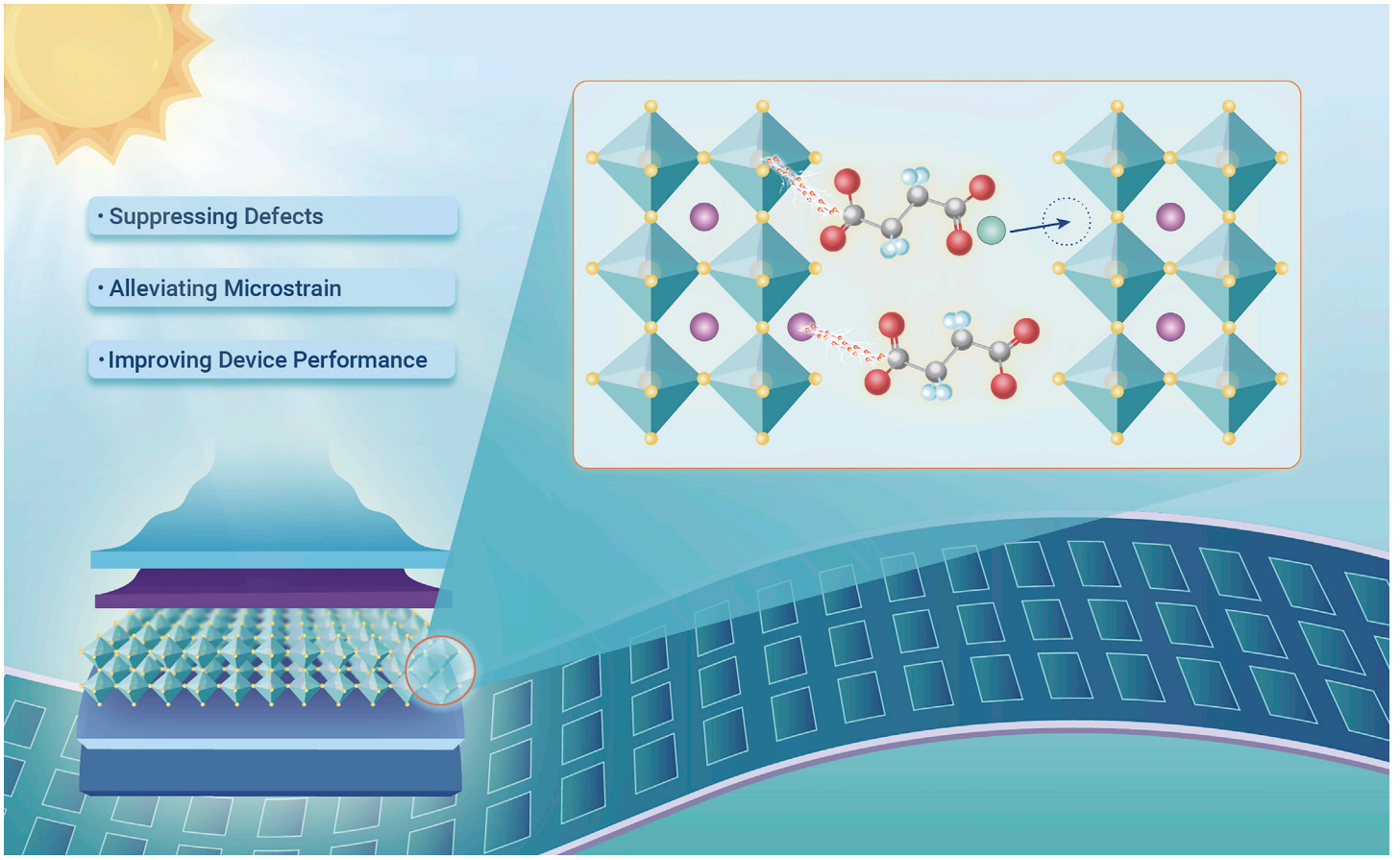

PUBLIC SUMMARY

- FPSCs hold promise as power sources for flexible electronics and spacecraft
- Succinate additives enable high-quality perovskite films with reduced microstrain
- An efficiency of 25.4% has been achieved for perovskite solar cells
- An efficiency of 23.6% has been achieved for FPSCs with excellent durability

Article

The Innovation

Multifunctional succinate additive for flexible perovskite solar cells with more than 23% power-conversion efficiency

Minghao Li,[1] Junjie Zhou,[1] Liguo Tan,[1] Hang Li,[1] Yue Liu,[1] Chaofan Jiang,[1] Yiran Ye,[1] Liming Ding,[2] Wolfgang Tress,[3] and Chenyi Yi[1,*]

[1]State Key Laboratory of Power System, Department of Electrical Engineering, Tsinghua University, Beijing 100084, China

[2]Center for Excellence in Nanoscience (CAS), Key Laboratory of Nanosystem and Hierarchical Fabrication (CAS), National Center for Nanoscience and Technology, Beijing 100190, China

[3]Institute of Computational Physics (ICP), ZHAW School of Engineering, Wildbachstr. 21, Winterthur 8400, Switzerland

*Correspondence: yicy@tsinghua.edu.cn

Received: June 9, 2022; Accepted: August 31, 2022; Published Online: September 6, 2022; https://doi.org/10.1016/j.xinn.2022.100310

Citation: Li M., Zhou J., Tan L., et al., (2022). Multifunctional succinate additive for flexible perovskite solar cells with more than 23% power-conversion efficiency. The Innovation **3(6)**, 100310.

Flexible perovskite solar cells (FPSCs) have emerged as power sources in versatile applications owing to their high-efficiency characteristics, excellent flexibility, and relatively low cost. Nevertheless, undesired strain in perovskite films greatly impacts the power-conversion efficiency (PCE) and stability of PSCs, particularly in FPSCs. Herein, a novel multifunctional organic salt, methylammonium succinate, which can alleviate strain and reinforce grain boundaries, was incorporated into the perovskite film, leading to relaxed microstrain and a lower defect concentration. As a result, a PCE of 25.4% for rigid PSCs and a record PCE of 23.6% (certified 22.5%) for FPSCs have been achieved. In addition, the corresponding FPSCs exhibited excellent bending durability, maintaining ~85% of their initial efficiency after bending at a 6 mm radius for 10 000 cycles.

INTRODUCTION

Perovskite solar cells (PSCs) have emerged as a cost-effective photovoltaic technology, as is obvious from the power-conversion efficiency (PCE), which has surpassed 25.7%.[1–4] With a high power-to-weight ratio and excellent flexibility, flexible PSCs (FPSCs) hold promise as power sources for flexible electronic devices, wearable equipment, and spacecraft.[5] With the experience accumulated in rigid PSCs, the PCE of FPSCs has reached over 22% in small areas[6,7] and 15% in large areas.[8,9] In addition, an increasing number of researchers have begun to explore the industrial roll-to-roll fabrication of FPSCs,[10,11] showing a promising future in flexible photovoltaic applications.

However, the PCE of FPSCs still lags far behind that of rigid PSCs, which can be mainly attributed to the inferior perovskite thin film quality on flexible substrates compared with that of glass substrates. The difference in the physical properties of glass substrates and flexible plastic substrates, such as thermal properties and surface roughness, increases the difficulty in obtaining high-quality perovskite thin films on plastic substrates.[12] Additives comprising small molecules and polymers were employed in the perovskite precursor to regulate the perovskite crystallization process,[13] improve crystallization, strengthen the perovskite crystals,[14] and passivate defects.[15]

Due to their polycrystalline nature, perovskite films also suffer from the influence of strain on the optoelectronic properties and stability.[16,17] The residual strain is related to the stability of the perovskite[18] and usually accelerates its degradation by increasing ion migration and reducing perovskite structural stability.[19] The microstrain, which originates from local lattice mismatch or misorientation and is related to the local lattice disorder and defects,[20] is highly detrimental to the perovskite film and thus urgently needs to be mitigated. Although modifying the perovskite lattice by cation doping, such as Cd^{2+}[21] and MDA^{2+},[22] has been demonstrated to lower microstrain for efficient and stable PSCs, the strain related to environmental effects such as bending, which is extremely important for FPSCs, cannot be alleviated by the above-mentioned method.

In this work, we judiciously designed a novel multifunctional additive, methylammonium succinate (MS), to alleviate strain and passivate interface defects in a perovskite film. It has been reported that FAI-terminated surfaces and PbI_2-terminated surfaces are stable surfaces in $FAPbI_3$ grains.[23] The two terminal carboxyl groups in MS can form hydrogen bonds with formamidine (FA) with two neighboring perovskite grains, while the ethylene group between the two carboxyl groups provides flexibility to release the strain caused by environmental effects such as thermal stress and bending of flexible devices, leading to perovskite films with reduced defects and enhanced durability. In addition, the carboxyl group can coordinate with the dangling Pb^{2+} present at the surface of perovskite grains, and the MA^+ can compensate for the A position vacancy in the ABX_3 perovskite, reducing the number of defects. As a result, we achieved a high PCE of 25.4% and 23.6% (certified 22.5%) for rigid and flexible PSCs, respectively, which is the highest reported PCE for FPSCs (Figure 1A) to date. In addition, the bilateral anions bind strongly with the perovskite grain surfaces, strengthening the grain boundaries (Figure 1B) and releasing the strain during the bending process. Therefore, the FPSCs exhibited improved bending durability, retaining ~85% of their initial efficiency after 10 000 bending cycles (at a 6 mm radius).

RESULTS AND DISCUSSION

The grain boundaries of perovskite thin films are rich in defects and the start points of the cracks, corrosion, and decomposition. The multifunctional additive MS was designed to heal the defects and strengthen the grain boundaries by interacting with two adjacent grain boundaries. With two terminal carboxyl groups, the succinate can bond with FA^+ cations via hydrogen bonds and coordinate with dangling Pb^{2+} in the grain boundaries. To investigate the effect of the MS additives, $FAPbI_3$ perovskite thin films were fabricated by a conventional sequential deposition method as previously reported.[24,25] The acquired perovskite thin films are denoted "control" and "MS-perovskite" for the films without and with MS additive (in PbI_2 solution), respectively. The surface scanning electron microscopy images of the control and MS-perovskite film morphologies are shown in Figures 2A and 2B. A small amount (~0.4 mol %) of MS additive resulted in a smoother surface, and the holes sighted in the control film were diminished. The cross-sectional images (Supplemental Figure 1) show that more grain boundaries exist near the control perovskite/SnO_2 interface, while the MS-perovskite film looks more uniform.

Detailed studies of the photophysical properties of the films indicate that MS incorporation improves the perovskite film quality without sacrificing light absorption. The absorption spectra (Figure 2C) and extracted band gap from the Tauc plot (Supplemental Figure 2) are almost identical for both films. This means that the MS additive did not compromise the light absorbing and absorption edge of the $FAPbI_3$ perovskite thin film. Photoluminescence (PL) spectra did not show any obvious peak shift either (Figure 2D). However, the MS-perovskite sample demonstrates a stronger PL intensity and longer PL lifetime (τ_{avg} = 867.1 versus 659.6 ns for the control sample; Figure 2E), revealing a reduced defect concentration in the perovskite film after MS incorporation. These results indicate that the MS molecule contributed to an improved thin film quality of the $FAPbI_3$ perovskite films.

Figure 2F shows the X-ray diffraction (XRD) patterns of the control and MS-modified films on the FTO substrates. It should be noted that residual PbI_2 is common in two-step-processed perovskite films.[26,27] On the other hand, the XRD patterns show no detectable peak shift or new peak arising in the MS-modified film. Therefore, we speculate that the MS molecule should not be incorporated into the $FAPbI_3$ lattice

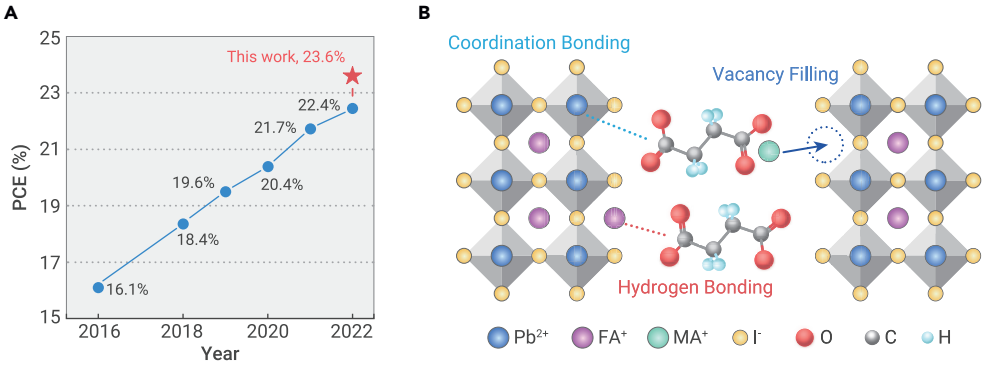

Figure 1. PCE result and the functions of the MS additive (A) Summarized PCE development of FPSCs with this work highlighted. **(B)** Proposed mechanism of the bilateral MS molecule at the perovskite grain boundaries.

but is mainly located in the grain boundaries. The bilateral structure of the MS molecule enables it to bond from both sides. Nuclear magnetic resonance (NMR) measurements were performed to elucidate the interaction mechanism between the MS molecule and the $FAPbI_3$ perovskite. As illustrated in the ^{1}H-NMR spectra (Figure 3A), for the two parts of the MS molecule, the MA^+ cation tends to interact with the inorganic PbI_2, as indicated by the shift of $-CH_3$ groups at approximately 2.3 ppm after mixing PbI_2 in the precursor solution. On the other hand, the $succinate^{2-}$ anion prefers to bond with the FA^+ cation via N–H ⋯ O hydrogen bonding, as indicated by the prominent shift of the resonance peak of the $-NH_2$ groups in FA^+. The shift of the COO^- group in the ^{13}C-NMR spectra (Figure 3B) indicates the interaction between Pb^{2+} and $succinate^{2-}$ anions. In a word, the NMR results indicate that $succinate^{2-}$ can bond with both FA^+ and Pb^{2+}. To compare the strength of the interactions, we calculated the absorption energy of succinate anions on the two kinds of perovskite surfaces (FAI terminated and PbI_2 terminated) by density functional theory. Negative absorption energy values are obtained in both situations, −4.86 eV in the FAI-terminated state and −4.16 eV in the PbI_2-terminated situation, which indicates a stronger interaction between the succinate anion and FA^+ cations. We speculated that MS interacts more with FA-related defects by forming hydrogen bonds with FA cations, suppressing the formation of FA vacancies.

To evaluate the effects of MS additives on the perovskite crystal structure, we first performed grazing incidence XRD characterizations to analyze the residual strain of the perovskite films.[28,29] Both control and MS-perovskite were almost strain free, while MS-perovskite showed a slightly compressed manner (Supplemental Figure 3). We consider this reasonable because residual strain is affected by the thermal expansion mismatch between perovskite and substrates,[30] while the perovskite composition,

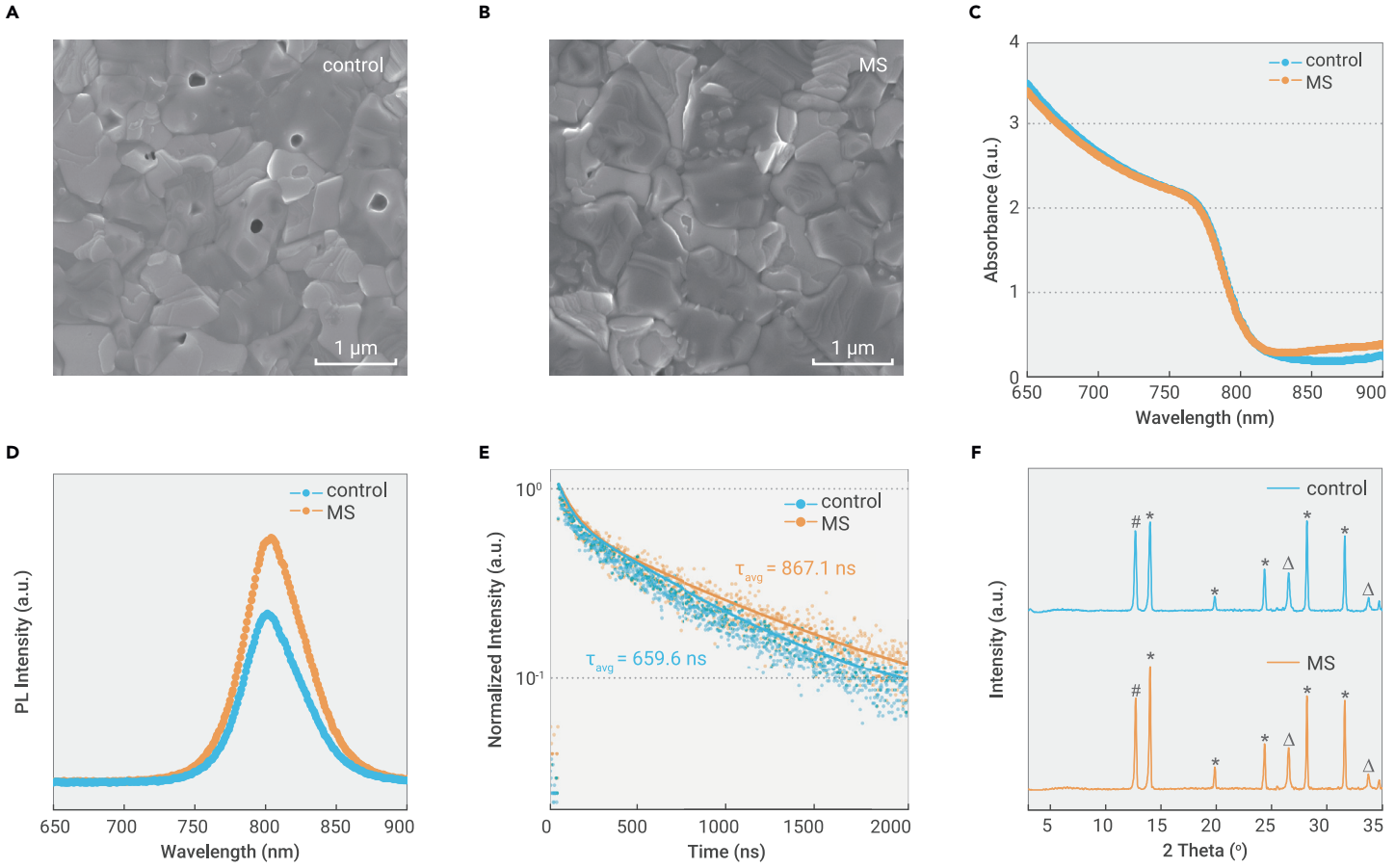

Figure 2. Perovskite thin film characterization (A–F) Scanning electron microscopy (SEM) images of top-view morphology **(A and B)**, UV–visible spectra **(C)**, static photoluminescence spectra **(D)**, time-resolved photoluminescence decay **(E)**, and X-ray diffraction pattern **(F)** of the control and MS-perovskite films (# denotes the PbI_2 phase, * denotes the $FAPbI_3$ perovskite phase, and Δ denotes the FTO substrate).

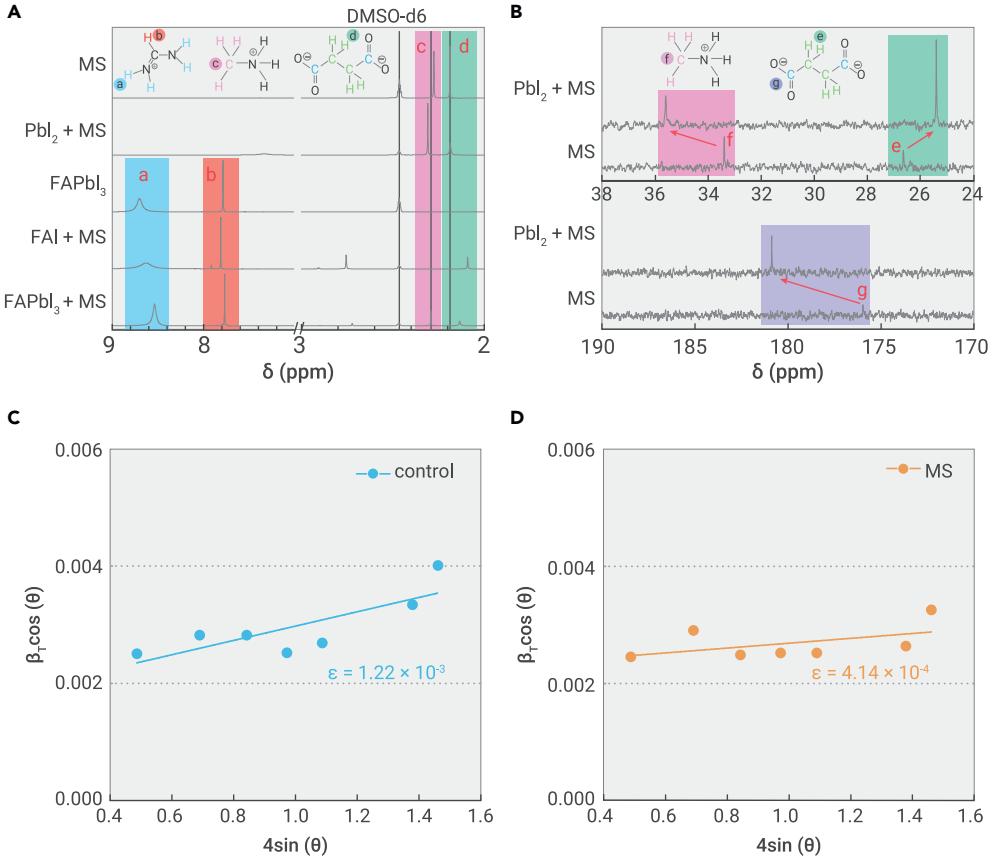

Figure 3. Interaction between the MS molecule and $FAPbI_3$ perovskite (A) ^{1}H-NMR result reveals that MS interacts with Pb^{2+} ions (MA^+ cations) and FA^+ ions ($succinate^{2-}$ anions). **(B)** ^{13}C-NMR result reveals that $-COO^-$ groups interact with PbI_2. **(C and D)** Microstrains in control and MS-perovskite thin films.

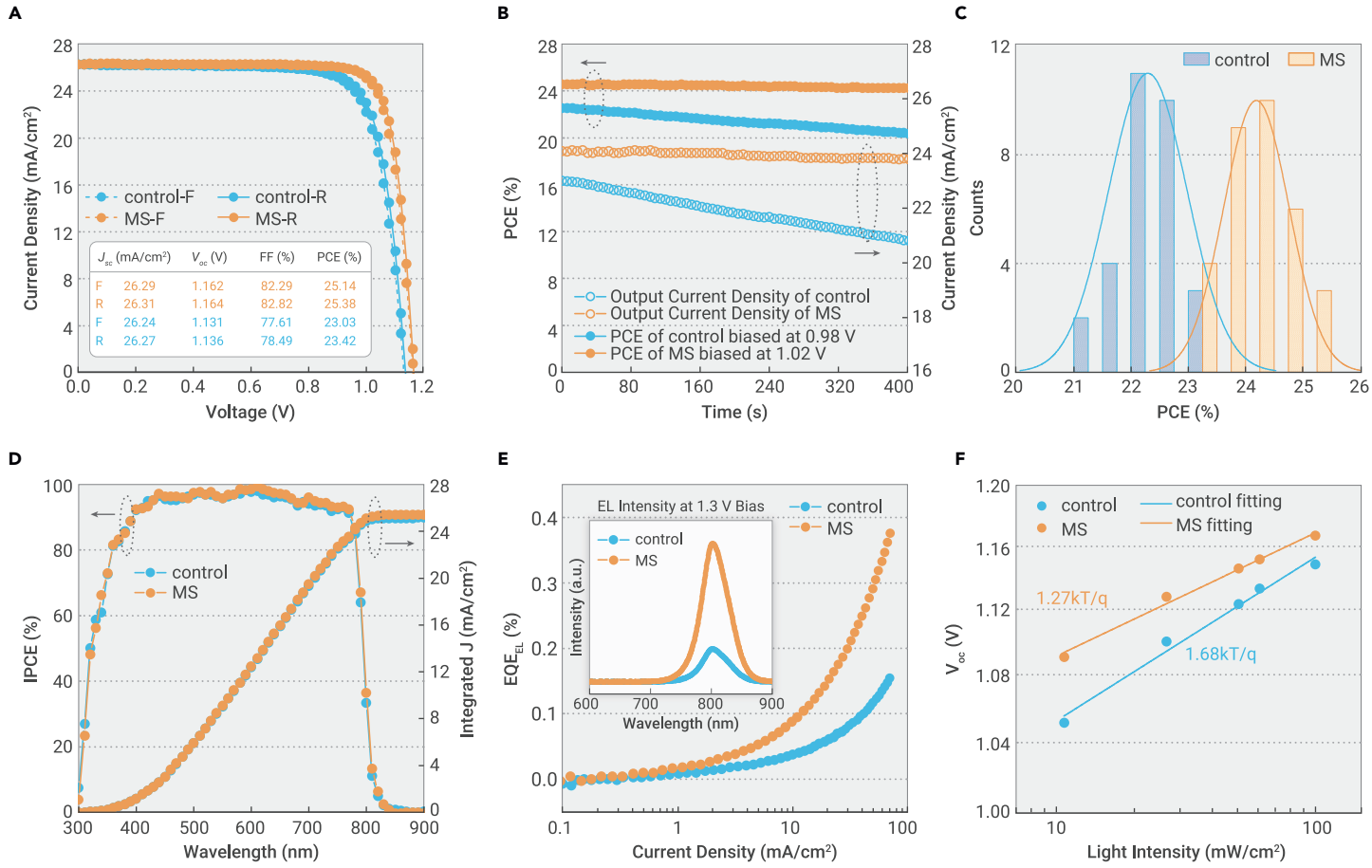

Figure 4. Photovoltaic characterization of the PSCs on glass substrates (A) *J-V* curves and photovoltaic metrics of the champion control and MS-PSCs. **(B)** Stable power output of the champion control and MS-PSCs at 0.98 and 1.02 V, respectively. **(C)** PCE distribution of control and MS-PSCs. **(D)** IPCE and the integrated J_{sc} curves of the control and MS-PSCs. **(E)** EQE_{EL} at different current densities and EL spectra of the control and MS-PSCs. **(F)** V_{oc} versus light intensity and linear fit for the control and MS-PSCs.

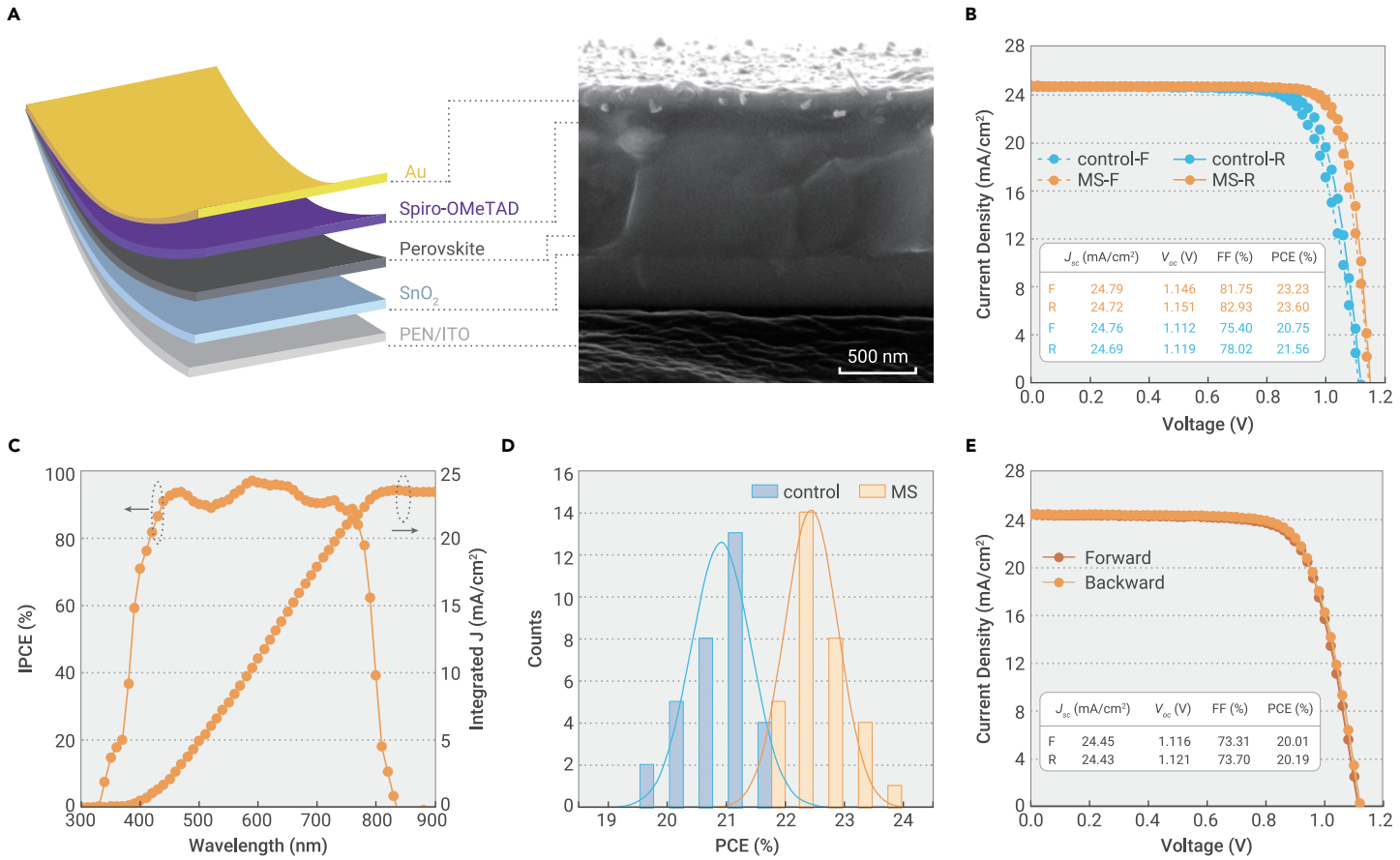

Figure 5. Photovoltaic characterization of the FPSCs (A) Device structure and the cross-sectional SEM image of the MS-FPSC. **(B)** *J-V* curves and photovoltaic metrics of the champion FPSCs. **(C)** IPCE and the integrated J_{sc} of the champion MS-FPSC. **(D)** Statistical distribution of the PCE of control and MS-FPSCs. **(E)** *J-V* curve of the 1 cm^2 aperture area MS-FPSC.

substrates, and annealing process were all the same in our case. We further analyzed the microstrain in the perovskite films through the Williamson-Hall equation:[31]

$$\beta_T \cos\theta = \varepsilon (4 \sin\theta) + \frac{K\lambda}{D},$$

where β_T is the full width at half maximum of the perovskite peaks in the XRD patterns, θ is the diffraction angle, K is the shape factor, λ is the wavelength of the X-ray source, and D is the crystallite size. The equation represents a linear relationship between $\beta_T \cos\theta$ and 4 sin θ, and the slope ε extracted here reveals the microstrain in the films. The MS additive effectively reduced the microstrain in the $FAPbI_3$ thin films from 1.22×10^{-3} to 4.14×10^{-4} (Figures 3C and 3D). As indicated by NMR measurements, the succinate anions can bond with FA^+ and Pb^{2+} atoms, which in turn can potentially suppress lattice defects and distortion at the grain boundaries, which will be beneficial to alleviate the microstrain in the perovskite films.[20] To exclude the crystalline size effect on the peak broadening of XRD patterns, we estimated the averaged crystalline sizes through the Scherrer equation:[22]

$$D = \frac{K\lambda}{\beta \cos\theta}.$$

The averaged crystalline sizes barely changed from 55.2 to 56.3 nm (Supplemental Table 5). Therefore, we concluded that the peak-broadening difference here mainly comes from the microstrain and that the crystal size effect contributes little. Previous reports have found that such microstrain in perovskite films is unfavorable for both PSC efficiency and stability.[21,22] The reduced microstrain is in line with the reduced defect concentration revealed by PL characterization,[22] which will be beneficial for the performance enhancement of PSCs. We also performed strain analysis for the flexible devices. The residual strain of the perovskite films on flexible substrates is higher than that of rigid substrates, which might be related to the different film growth process, arising from the roughness difference of flexible and rigid substrates.[8] Compared with the pristine perovskite film, a slightly lower residual tensile strain is obtained in the MS-perovskite (Supplemental Figure 4), which is favorable for the FPSCs. As shown in Supplemental Figure 5, the XRD patterns show strong features of PEN substrates. Nevertheless, we can elucidate the microstrains by analyzing the perovskite peaks not overlapped with PEN with Williamson-Hall equation, showing a reduced microstrain for the MS-perovskite film (Supplemental Figure 6), which is favorable for the performances of the FPSCs.

The performances of the PSCs without and with MS incorporation were investigated by *J-V* characterization. Devices were fabricated based on the standard configuration using SnO_2 and spiro-OMeTAD as electron- and hole-transporting layers, respectively. The *J-V* curves of the champion control and MS-PSCs are shown in Figure 4A. The control device demonstrated a PCE of 23.4%. The MS-PSC reached a higher efficiency of 25.4%, with a short-circuit current density (J_{sc}) of 26.31 mA/cm^2, an open-circuit voltage (V_{oc}) of 1.164 V, and fill factor of 82.82%. The unencapsulated MS-PSC showed a stable power output at 1.02 V bias with a PCE of ~24.5% during the recorded 400 s in air (Figure 4B), reflecting the excellent short-term stability, while the control device dropped obviously from 22.5% to ~20.5%. Moreover, the statistical distribution confirmed the overall improvement brought by MS incorporation, especially in the PCE (Figure 4C) and V_{oc} (Supplemental Figure 7).

The incident photon-to-current conversion efficiency (IPCE) results shown in Figure 4D verified the measured J_{sc}. The IPCE spectra of the control and modified devices show only small differences. The integrated J_{sc} of the control and MS-PSCs are 25.15 and 25.54 mA/cm^2, respectively, which matches well with the *J-V* analysis. Electroluminescence (EL) was conducted to reveal the nonradiative recombination in the PSCs (Figure 4E). The MS device not only shows a more

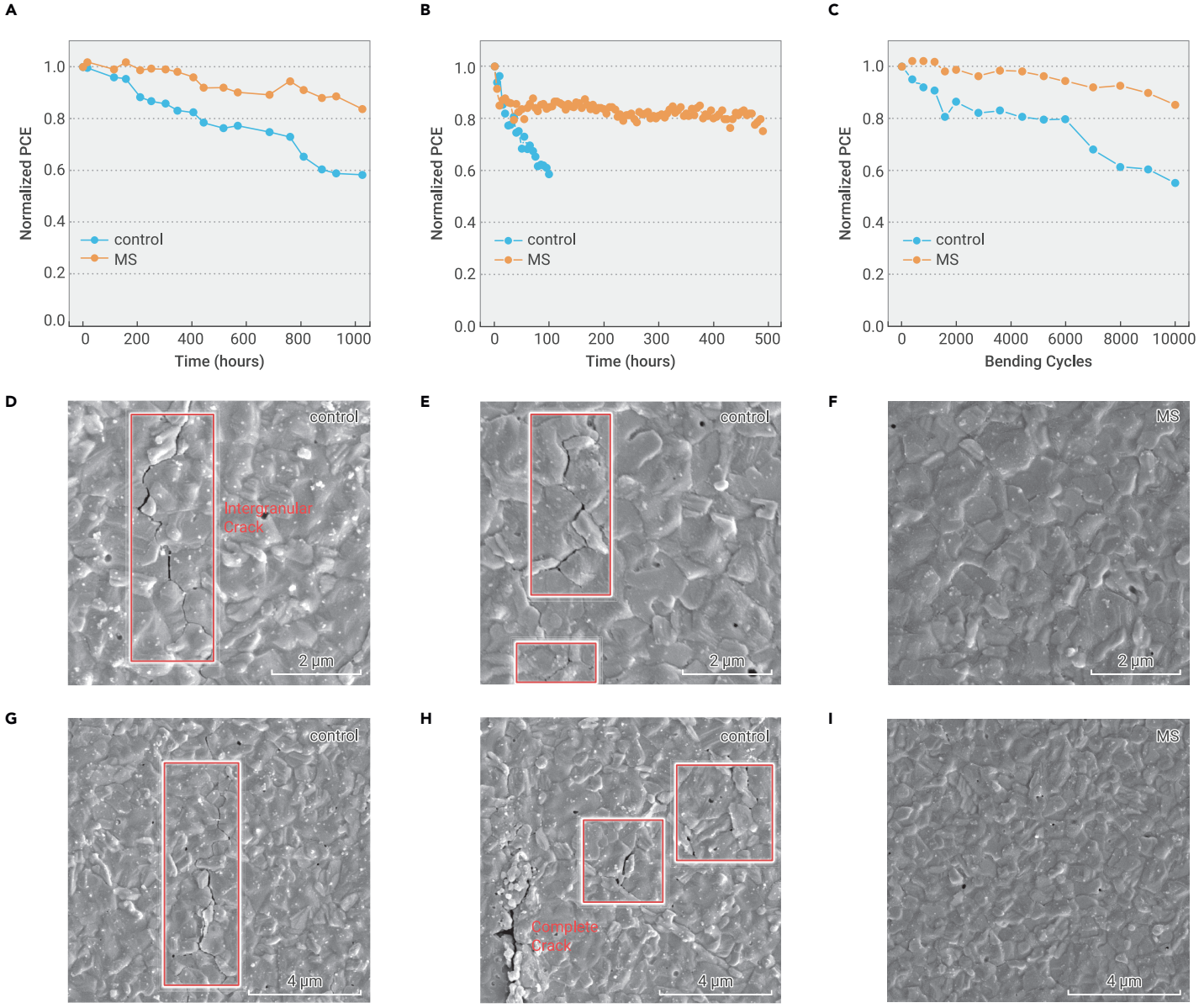

Figure 6. Tracked stability of the solar cell devices (A) The stability of the unencapsulated control and MS-PSCs under ~30% relative humidity. **(B)** Long-term stability of the unencapsulated PSCs under continuous light irradiation in a N_2 atmosphere. **(C)** The bending stability of FPSCs (R = 6 mm, ~30% relative humidity, ~25°C). **(D–I)** Top-view SEM images of the perovskite film from FPSCs after 10 000 bending cycles at 6 mm, with the Au electrode removed by tape and spiro-OMeTAD removed by chlorobenzene.

pronounced electroluminescence intensity at 1.3 V but also demonstrates a higher external quantum efficiency (EQE) for all applied currents, indicating suppressed nonradiative recombination in the perovskite. The relationship between V_{oc} and the light intensity is investigated to determine the ideality factor n, which is related to trap-assisted recombination. The lower n (1.27) of the MS device than that of the control device (1.68) indicates the reduced trap-assisted recombination of the MS device (Figure 4F). Moreover, transient photovoltage decay (Supplemental Figure 8A) and space-charge-limited current measurements (Supplemental Figure 9) further support the reduced trap densities and improved V_{oc} and device performance.

The bilateral structure of the MS molecule, which is able to bind strongly with grain boundaries and relax microstrain, should be beneficial for the mechanical durability of perovskite films. This inspired us to fabricate MS-perovskite-based FPSC devices using PEN/ITO substrates (Figure 5A). Figure 5B demonstrates the *J-V* curves and photovoltaic metrics for the champion FPSC with and without MS incorporation. The champion MS-FPSC had a maximum PCE of 23.6% in the reserve scan, along with a J_{sc} of 24.72 mA cm^{-2}, a V_{oc} of 1.151 V, and a fill factor of 82.93%, exceeding the 21.6% PCE of champion control. This outstands as the highest PCE reported for FPSCs.[6,7,9,32,33] The champion device showed little hysteresis, which reached 23.2% in the forward scan. The integrated J_{sc} deduced from the IPCE measurement also reached 23.44 mA cm^{-2} (Figure 5C), which is consistent with that acquired from *J-V* analysis. To further verify the measured efficiency, we sent one of our MS-FPSCs for certification, which displays a certified efficiency of 22.5% with a stabilized power output efficiency of ~22.0% at 1.01 V bias (Supplemental Figure 13). The quasi-steady-state and stabilized efficiency both rank as the highest in all certified FPSCs.[6,7] The overall improvement of the FPSC performance is outstanding (Figure 5D), in line with the results obtained on rigid PSCs. The application of the MS additive also demonstrated over 20% PCE for the large-area 1 cm^2 device (Figure 5E), which could be higher with further optimization.[4]

The stability of the PSCs was measured, and the MS-PSCs demonstrated improved resistance to humidity and operation conditions. We first tracked the shelf-life stability of the unencapsulated PSCs. After 1000 h of storage under ~30% relative humidity, the control device

lost ~40% of the initial PCE, while the MS device showed a slower degradation of ~15% (Figure 6A). The enhanced humidity resistance could be attributed to the hydrophobic alkyl chain located at the grain boundaries, which is the main channel for water infiltration. Unencapsulated devices were also aged under continuous light soaking in our homemade maximum power point tracking system at 25°C in a N_2 atmosphere to further assess the long-term operational stability (Figure 6B). Despite experiencing a rapid burn in, the power output of the MS-PSC maintained >80% of the initial PCE for ~500 h. However, the PCE of the control device dropped quickly to ~60% of its initial value after 100 h, in good agreement with the short-term stability displayed in Figure 4B. It is well known that the degradation process in perovskite starts mainly from the grain boundaries.[34] As revealed by the PL and NMR measurements, the MS additive not only reduced the defects in the bulk perovskite but also strengthened the perovskite lattice structure via hydrogen bonding at the grain boundaries, which contributed to the enhanced operational stability.[35,36]

For mechanical stability, we performed a continuous bending test to evaluate the mechanical durability of FPSC devices and recorded their efficiency change during the test. The control FPSC gradually dropped to 60% of the initial PCE after 10 000 bending cycles (bending radius 6 mm), while the MS-FPSC retained ~85% of its initial PCE (Figure 6C), indicating improved mechanical durability of the modified devices. The improved mechanical stability of the MS-FPSC could be attributed to the strengthened grain boundaries and relaxed microstrain, which inhibited perovskite fracture and defect formation.[21,37] We further observed the morphology change of the perovskite film of the devices after the cyclic bending test. The metal electrode and the spiro-OMeTAD layer were removed to expose the perovskite layer. The crack in the control film is obvious and mainly develops inter granularly (Figures 6D and 6E). In contrast, the MS-perovskite film shows no cracks (Figures 6F and 6I). The well-maintained film morphology could also inhibit moisture infiltration in the ambient environment in our bending,[32] which further confirmed the improved stability of the MS-FPSCs. In addition, we performed a bending test with a radius of 5 mm. Although both devices degraded faster than that of the 6 mm bending test, possibly due to ITO fracture, the MS-FPSC showed a T80 4 times longer than that of the control FPSC (Supplemental Figure 15).

CONCLUSION

In conclusion, we demonstrated the incorporation of bilateral MS molecules into a perovskite thin film for high performance and stable PSCs. The additive molecule effectively reduces the microstrain in the $FAPbI_3$ perovskite thin film, resulting in improved quality and reduced defect concentration of the thin film. High-efficiency PSCs were fabricated on both rigid substrates and flexible PEN substrates. Specifically, FPSCs with MS incorporation showed an impressively high efficiency of 23.6% (certified 22.5%), which ranks as the highest value in the reported literature to date. Furthermore, MS-FPSCs showed improved bending durability, retaining ~85% of the initial efficiency after 10 000 bending cycles. The efficiency and mechanical stability of the FPSCs are closely related to the microstrain of the perovskite film. This work provides a new solution to reduce microstrain by using a multifunctional organic additive that does not incorporate into the perovskite lattice but strengthens the grain boundaries and heals the defects. A variety of new molecules with similar supermolecular interactions such as hydrogen bond, coordination, and halogen bond can be designed to alleviate microstrain, which will further improve the performances and stability of FPSCs, promoting the large-scale application of this power sources.

METHODS

Please refer to the supplemental information for details on methods.

REFERENCES

1. NREL best research-cell efficiency chart. https://www.nrel.gov/pv/assets/pdfs/best-research-cell-efficiencies-rev220126.pdf.
2. Zhang, F., Park, S.Y., Yao, C., et al. (2022). Metastable Dion-Jacobson 2D structure enables efficient and stable perovskite solar cells. Science ***375***, 71–76.
3. Li, X., Zhang, W., Guo, X., et al. (2022). Constructing heterojunctions by surface sulfidation for efficient inverted perovskite solar cells. Science ***375***, 434–437.
4. Wang, S., Tan, L., Zhou, J., et al. (2022). Over 24% efficient MA-free $Cs_xFA_{1-x}PbX_3$ perovskite solar cells. Joule ***6***, 1344–1356.
5. Hu, Y., Niu, T., Liu, Y., et al. (2021). Flexible perovskite solar cells with high power-per-weight: progress, application, and perspectives. ACS Energy Lett. ***6***, 2917–2943.
6. Zheng, Z., Li, F., Gong, J., et al. (2022). Pre-buried additive for cross-layer modification in flexible perovskite solar cells with efficiency exceeding 22. Adv. Mater. ***34***, 2109879.
7. Yang, L., Feng, J., Liu, Z., et al. (2022). Record-efficiency flexible perovskite solar cells enabled by multifunctional organic ions interface passivation. Adv. Mater. ***34***, 2201681.
8. Dai, X., Deng, Y., Van Brackle, C.H., et al. (2019). Scalable fabrication of efficient perovskite solar modules on flexible glass substrates. Adv. Energy Mater. ***10***, 1903108.
9. Chung, J., Shin, S.S., Hwang, K., et al. (2020). Record-efficiency flexible perovskite solar cell and module enabled by a porous-planar structure as an electron transport layer. Energy Environ. Sci. ***13***, 4854–4861.
10. Othman, M., Zheng, F., Seeber, A., et al. (2022). Millimeter-sized clusters of triple cation perovskite enables highly efficient and reproducible roll-to-roll fabricated inverted perovskite solar cells. Adv. Funct. Mater. ***32***, 2110700.
11. Li, H., Zuo, C., Angmo, D., et al. (2022). Fully roll-to-roll processed efficient perovskite solar cells via precise control on the morphology of PbI_2:CsI layer. Nano-Micro Lett. ***14***, 79.
12. Jung, H.S., Han, G.S., Park, N.-G., and Ko, M.J. (2019). Flexible perovskite solar cells. Joule ***3***, 1850–1880.
13. Feng, J., Zhu, X., Yang, Z., et al. (2018). Record efficiency stable flexible perovskite solar cell using effective additive assistant strategy. Adv. Mater. ***30***, e1801418.
14. Hu, X., Huang, Z., Li, F., et al. (2019). Nacre-inspired crystallization and elastic "brick-and-mortar" structure for a wearable perovskite solar module. Energy Environ. Sci. ***12***, 979–987.
15. Yang, L., Xiong, Q., Li, Y., et al. (2021). Artemisinin-passivated mixed-cation perovskite films for durable flexible perovskite solar cells with over 21% efficiency. J. Mater. Chem. ***9***, 1574–1582.
16. Liu, D., Luo, D., Iqbal, A.N., et al. (2021). Strain analysis and engineering in halide perovskite photovoltaics. Nat. Mater. ***20***, 1337–1346.
17. Cheng, Y., and Ding, L. (2021). Pushing commercialization of perovskite solar cells by improving their intrinsic stability. Energy Environ. Sci. ***14***, 3233–3255.
18. Rolston, N., Bush, K.A., Printz, A.D., et al. (2018). Engineering stress in perovskite solar cells to improve stability. Adv. Energy Mater. ***8***, 1802139.
19. Zhao, J., Deng, Y., Wei, H., et al. (2017). Strained hybrid perovskite thin films and their impact on the intrinsic stability of perovskite solar cells. Sci. Adv. ***3***, eaao5616.
20. Wu, J., Liu, S.-C., Li, Z., et al. (2021). Strain in perovskite solar cells: origins, impacts and regulation. Natl. Sci. Rev. ***8***, nwab047.
21. Saidaminov, M.I., Kim, J., Jain, A., et al. (2018). Suppression of atomic vacancies via incorporation of isovalent small ions to increase the stability of halide perovskite solar cells in ambient air. Nat. Energy ***3***, 648–654.
22. Kim, G., Min, H., Lee, K.S., et al. (2020). Impact of strain relaxation on performance of α-formamidinium lead iodide perovskite solar cells. Science ***370***, 108–112.
23. Oner, S.M., Sezen, E., Yordanli, M.S., et al. (2022). Surface defect formation and passivation in formamidinium lead triiodide ($FAPbI_3$) perovskite solar sell absorbers. J. Phys. Chem. Lett. ***13***, 324–330.
24. Zhou, J., Li, M., Wang, S., et al. (2022). 2-CF_3-PEAI to eliminate Pb^0 traps and form a 2D perovskite layer to enhance the performance and stability of perovskite solar cells. Nano Energy ***95***, 107036.
25. Li, M., Zhou, J., Tan, L., et al. (2022). Brominated PEAI as multi-functional passivator for high-efficiency perovskite solar cell. Energy Environ. Mater, eem2.12360.
26. Yang, X., Fu, Y., Su, R., et al. (2020). Superior carrier lifetimes exceeding 6 μs in polycrystalline halide perovskites. Adv. Mater. ***32***, 2002585.
27. Xue, J., Wang, R., Chen, X., et al. (2021). Reconfiguring the band-edge states of photovoltaic perovskites by conjugated organic cations. Science ***371***, 636–640.
28. Zhu, C., Niu, X., Fu, Y., et al. (2019). Strain engineering in perovskite solar cells and its impacts on carrier dynamics. Nat. Commun. ***10***, 815.
29. Li, F., Deng, X., Qi, F., et al. (2020). Regulating surface termination for efficient inverted perovskite solar cells with greater than 23% efficiency. J. Am. Chem. Soc. ***142***, 20134–20142.
30. Xue, D.-J., Hou, Y., Liu, S.-C., et al. (2020). Regulating strain in perovskite thin films through charge-transport layers. Nat. Commun. ***11***, 1514.
31. Williamson, G.K., and Hall, W.H. (1953). X-ray line broadening from filed aluminium and wolfram. Acta Metall. ***1***, 22–31.
32. Dong, Q., Chen, M., Liu, Y., et al. (2021). Flexible perovskite solar cells with simultaneously improved efficiency, operational stability, and mechanical reliability. Joule ***5***, 1587–1601.
33. Wu, S., Li, Z., Zhang, J., et al. (2021). Low-bandgap organic bulk-heterojunction enabled efficient and flexible perovskite solar cells. Adv. Mater. ***33***, 2105539.
34. Jeong, J., Kim, M., Seo, J., et al. (2021). Pseudo-halide anion engineering for α-$FAPbI_3$ perovskite solar cells. Nature ***592***, 381–385.
35. Li, X., Dar, M.I., Yi, C., et al. (2015). Improved performance and stability of perovskite solar cells by crystal crosslinking with alkylphosphonic acid omega-ammonium chlorides. Nat. Chem. ***7***, 703–711.
36. Bai, S., Da, P., Li, C., et al. (2019). Planar perovskite solar cells with long-term stability using ionic liquid additives. Nature ***571***, 245–250.
37. Huang, Z., Hu, X., Liu, C., et al. (2017). Nucleation and crystallization control via polyurethane to enhance the bendability of perovskite solar cells with excellent device performance. Adv. Funct. Mater. ***27***, 1703061.

ACKNOWLEDGMENTS

This work was supported by the National Natural Science Foundation of China (no. 21872080) and projects supported by the State Key Laboratory of Power System and

Generation Equipment (nos. SKLD21Z03 and SKLD20M03), the Chinese Thousand Talents Program for Young Professionals, and State Grid Corporation of China, National Bio Energy Co., Ltd. This work was also supported by grant no. 52789922000D, China Huaneng Group Co., Ltd., and grant no. HNKJ20-H88.

AUTHOR CONTRIBUTIONS

C.Y. conceived the idea and directed the project. M.L., J.Z., and L.T. performed the experiments. M.L. prepared the draft. All the authors participated in the discussion of the results and revision of the manuscript. The lead contact's websites are as follows: https://www.x-mol.com/groups/Tsinghua-EEA-312lab?lang=en and https://www.eea.tsinghua.edu.cn/en/faculties/yicy.htm.

DECLARATION OF INTERESTS

The authors declare no competing interests.

SUPPLEMENTAL INFORMATION

Supplemental information can be found online at https://doi.org/10.1016/j.xinn.2022.100310.

The Innovation, Volume *3*

Supplemental Information

Multifunctional succinate additive for flexible perovskite solar cells with more than 23% power-conversion efficiency

Minghao Li, Junjie Zhou, Liguo Tan, Hang Li, Yue Liu, Chaofan Jiang, Yiran Ye, Liming Ding, Wolfgang Tress, and Chenyi Yi

Supporting Information

Multifunctional succinate additive for flexible perovskite solar cells with more than 23% power conversion efficiency

Minghao Li[1], Junjie Zhou[1], Liguo Tan[1], Hang Li[1], Yue Liu[1], Chaofan Jiang[1], Yiran Ye[1], Liming Ding[2], Wolfgang Tress[3], Chenyi Yi[1,*]

[1] State Key Laboratory of Power System, Department of Electrical Engineering, Tsinghua University, Beijing, 100084, China.

[2] Center for Excellence in Nanoscience (CAS), Key Laboratory of Nanosystem and Hierarchical Fabrication (CAS), National Center for Nanoscience and Technology, Beijing 100190, China.

[3] Institute of Computational Physics (ICP) ZHAW School of Engineering Wildbachstr. 21, Winterthur 8400, Switzerland.

[*]Correspondence: yicy@tsinghua.edu.cn

Methods

Chemicals

The chemicals were purchased from commercial sources and used without further purification. MS was synthesized by first dissolving succinic acid in ethanol with vigorous stirring. Then, an excess of methylamine ethanol solution was added dropwise to the succinic acid solution and stirred for 2~3 hours. White participation appeared after stirring for a long time. The acquired powder was washed with diethyl ether several times to obtain pure MS.

Device Fabrication

FTO/glass substrates and PEN/ITO substrates were used for device fabrication and were first etched by laser and chemical etching (Zn/HCl), respectively. The flexible substrates were further attached onto FTO/glass substrates for mechanical support with PDMS.[1] All substrates were ultrasonically washed with detergent, deionized water, ethanol and isopropanol sequentially and then treated with UV-ozone for 20 min before electron transporting layer deposition. For FTO/glass substrates, a SnO_2 layer was deposited by chemical bath deposition as previously reported.[2] For flexible substrates, the conventional method was adopted by spin-coating the commercial SnO_2 nanoparticles (diluted 1:3) onto the substrates, followed by an annealing process at 150 ^oC for 30 min in ambient air. The process of perovskite thin film deposition, surface treatment and hole transporting layer deposition were all the same as we have reported previously.[3] In brief, after UV-ozone treatment, 1.5 M PbI_2 solution with 1~2 mol% CsI in DMF and DMSO (volume ratio 9:1) was first spun onto the SnO_2 layer at 1500 rpm. After annealing at 70 ^oC, organic ammonium salt (FAI: MAI: MACl = 90 mg: 6 mg: 9 mg) in IPA solution was then spun onto the PbI_2 layer at 2000 rpm. The obtained films were annealed at 150 ^oC for 15 min in an ambient environment. For the modified sample, MS were added to the PbI_2 precursor to obtain designated concentrations of MS-incorporated perovskite thin films. For the posttreatment process, the cooled perovskite films were treated with 10 mM 2-Br-PEAI/IPA solution at 4000 rpm and annealed at 100 ^oC for 10 min. For the hole transporting layer, spiro-OMeTAD solution was deposited at 4000 rpm for 20 s. Finally, back contact was deposited by thermally evaporating 80 nm Au. Anti-reflection film was deposited on the glass side of the device before measurement.

Characterization

The SEM images of the perovskite film were obtained on a Zeiss Merlin. An Agilent Cary 5000 UV-vis spectrophotometer was used to record the absorption spectra of the perovskite film. Photoluminescence and time-resolved PL decay results were collected on an Edinburgh FLSP920 system with an excitation source of 405 nm wavelength. Conventional XRD measurements of perovskite thin films were conducted on a Rigaku SmartLab (copper Kα, λ = 1.54 Å, 150 mA, 40 kV). GIXRD measurements were conducted using a Bruker D8 Advance (copper Kα, λ = 1.54 Å, 150 mA, 40 kV). A JEOL ECS-400 was utilized to collect the ^1H and ^{13}C NMR spectra of the samples in DMSO-d6.

Sun *J-V* measurements of the solar cells were performed under a Newport AAA solar simulator with a Keithley 2400 source meter. The light intensity was calibrated by an NREL certified silicon diode. An aperture area of 0.1 cm^2 or

1.0 cm^2 was achieved by using a dark metal mask with the designated area. The measurement was conducted in ambient air using unencapsulated devices. The stable output power of the devices was characterized by holding the device at a premeasured maximum power point bias voltage determined by the *J-V* measurement. The long-term stability of the devices (in N_2) under illumination was characterized with homemade multichannel MPPT instruments using an LED as the light source. The bending durability of the FPSCs was tested by homemade bending equipment with the corresponding bending radius, and the PCE was recorded after bending specific cycles.

DFT Calculations

The Vienna *Ab initio* Simulation Package (VASP) was employed to perform the first-principles calculations.[4] The Kohn-Sham equation was solved by using the plane wave basis set. The GGA-PBE exchange-correlation functional was selected to describe the electron interactions.[5] Valence-core interactions were described by projector-augmented-wave (PAW) pseudopotentials.[6] Grimme's DFT-D3 method was used for the van der Waals interaction correction.[7] The cutoff energy for the plane wave basis sets was 400 eV. Only the Γ-point was considered for calculations. All the optimizations were conducted until the residual of energy and forces decreased than $10^{-5}\ eV$ and $0.05\ eV/\text{Å}$, respectively. Two different perovskite surface situations (FAI-terminated and PbI_2 terminated) were modeled to evaluate the absorption energy of the succinate anions on the surfaces. The absorption energy is described by

$$E_{abs} = E_{MS+FAPbI_3} - E_{MS} - E_{FAPbI_3}$$

where E_{abs} is the absorption energy of the succinate anion, $E_{MS+FAPbI_3}$ is the energy of the whole system, and E_{MS} and E_{FAPbI_3} are the energies of the succinate anion and $FAPbI_3$ perovskite, respectively.

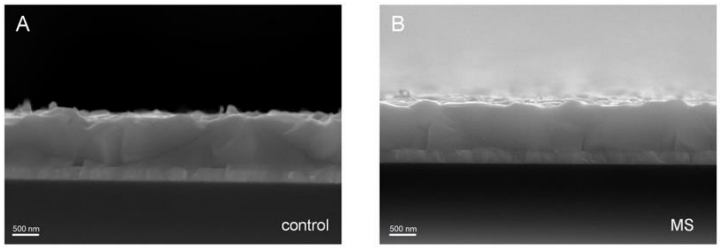

Figure S1. Cross-sectional SEM images of (A) Control, (B) MS-perovskite film.

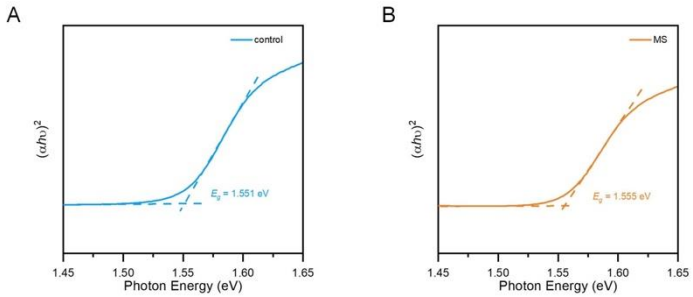

Figure S2. Tauc plot and acquired bandgap of the perovskite films from UV-vis characterization.

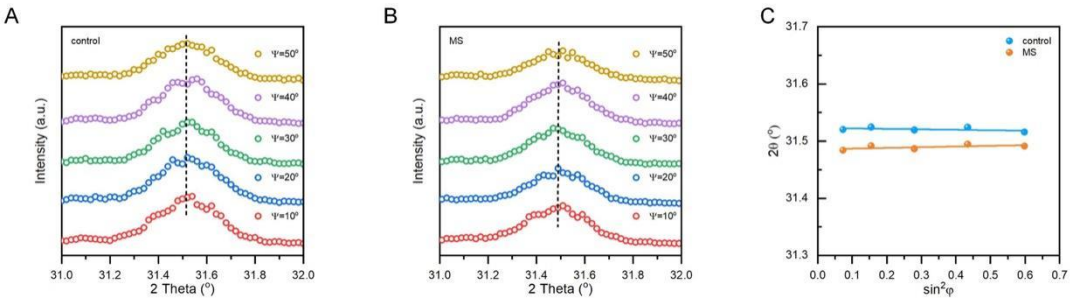

Figure S3. Residual strain analysis of the control and MS-perovskite on rigid FTO glass substrates. (A, B) GIXRD spectrum at different tilt angles for the (A) control and (B) MS perovskite. (C) Residual strain of the corresponding perovskite films.

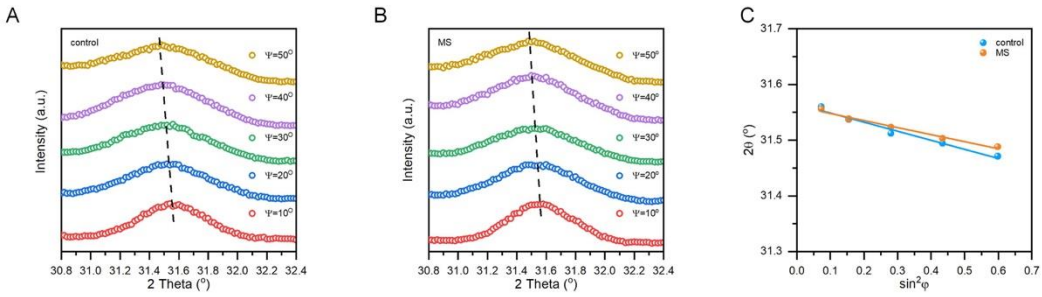

Figure S4. Residual strain analysis of the control and MS-perovskite on flexible substrates. (A, B) GIXRD spectrum at different tilt angles for the (A) control and (B) MS-perovskite. (C) Residual strain of the corresponding perovskite films.

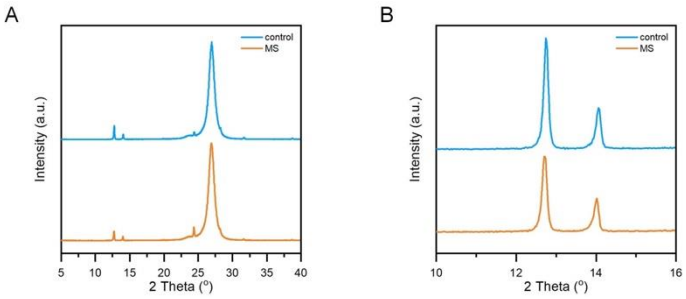

Figure S5. XRD spectra of the control and MS-perovskite thin films on PEN/ITO.

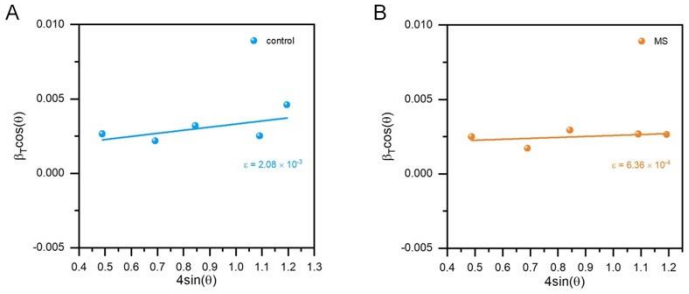

Figure S6. Microstrains in control and MS-perovskite on PEN/ITO substrates.

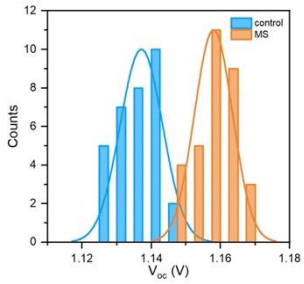

Figure S7. Open-circuit voltage (V_{oc}) distribution of the PSCs in the same batch.

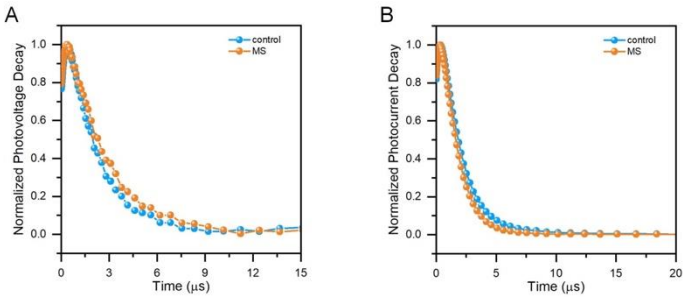

Figure S8. Normalized transient photovoltage and photocurrent decay of the control and MS-PSCs. The MS device demonstrates relatively slower photovoltage decay and faster photocurrent decay, in agreement with the increased V_{oc} and charge transport.

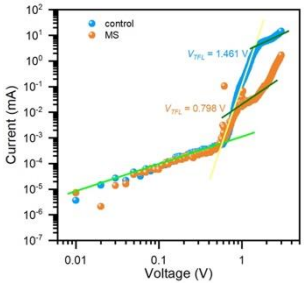

Figure S9. Space charge limited current (SCLC) measurements of the control and MS-perovskite incorporated electron only devices. Device structure: FTO/SnO_2/perovskite/PCBM/Au. The MS device shows a lower trap filling voltage. This trend supports that bulk defects are reduced due to MS incorporation.

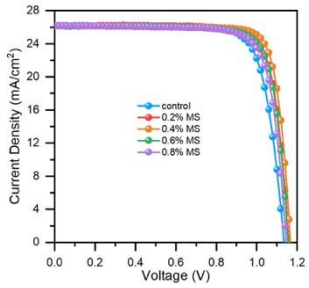

Figure S10. Typical *J-V* curves of rigid devices with different additive concentrations.

Table S1. Summary of the rigid device performance of the different MS concentrations.

MS concentration (%)	J_{sc} (mA/cm²)	V_{oc} (V)	FF (%)	PCE (%)
0	26.19	1.134	77.86	23.13
0.2	26.18	1.158	80.39	24.37
0.4	26.14	1.167	82.57	25.18
0.6	26.12	1.155	79.99	24.13
0.8	26.12	1.145	78.90	23.62

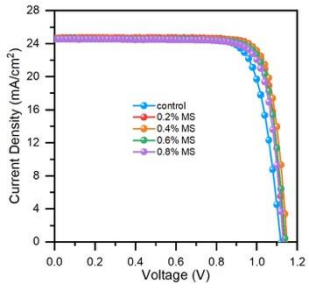

Figure S11. Typical J-V curves of flexible devices with different additive concentrations.

Table S2. Summary of the flexible device performance of the different MS concentrations.

MS concentration (%)	J_{sc} (mA/cm^2)	V_{oc} (V)	FF (%)	PCE (%)
0	24.69	1.119	78.02	21.56
0.2	24.64	1.146	79.99	22.59
0.4	24.60	1.149	81.93	23.17
0.6	24.56	1.141	81.14	22.74
0.8	24.53	1.131	80.52	22.34

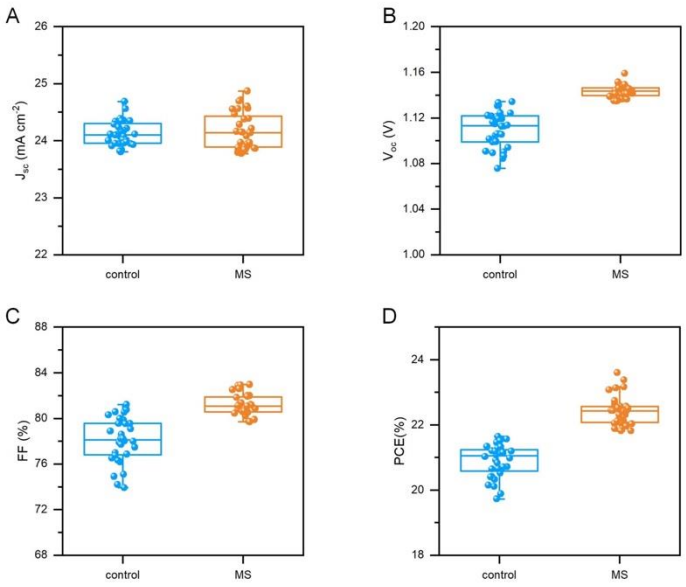

Figure S12. Statistical distribution of the photovoltaic metrics of the control and MS-FPSCs. (A) J_{sc}, (B) V_{oc}, (C) FF and (D) PCE.

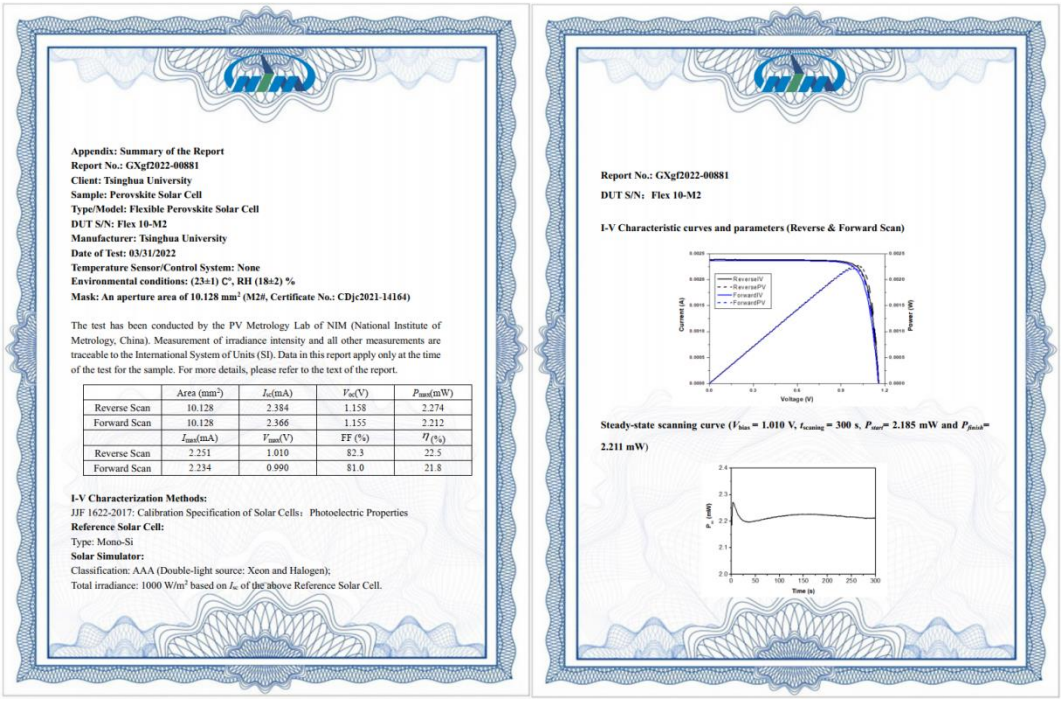

Appendix: Summary of the Report
Report No.: GXgf2022-00881
Client: Tsinghua University
Sample: Perovskite Solar Cell
Type/Model: Flexible Perovskite Solar Cell
DUT S/N: Flex 10-M2
Manufacturer: Tsinghua University
Date of Test: 03/31/2022
Temperature Sensor/Control System: None
Environmental conditions: (23±1) C°, RH (18±2) %
Mask: An aperture area of 10.128 mm² (M2#, Certificate No.: CDjc2021-14164)

The test has been conducted by the PV Metrology Lab of NIM (National Institute of Metrology, China). Measurement of irradiance intensity and all other measurements are traceable to the International System of Units (SI). Data in this report apply only at the time of the test for the sample. For more details, please refer to the text of the report.

	Area (mm²)	I_{sc}(mA)	V_{oc}(V)	P_{max}(mW)
Reverse Scan	10.128	2.384	1.158	2.274
Forward Scan	10.128	2.366	1.155	2.212
	I_{max}(mA)	V_{max}(V)	FF (%)	η (%)
Reverse Scan	2.251	1.010	82.3	22.5
Forward Scan	2.234	0.990	81.0	21.8

I-V Characterization Methods:
JJF 1622-2017: Calibration Specification of Solar Cells：Photoelectric Properties
Reference Solar Cell:
Type: Mono-Si
Solar Simulator:
Classification: AAA (Double-light source: Xeon and Halogen);
Total irradiance: 1000 W/m² based on I_{sc} of the above Reference Solar Cell.

Report No.: GXgf2022-00881
DUT S/N：Flex 10-M2

I-V Characteristic curves and parameters (Reverse & Forward Scan)

Steady-state scanning curve (V_{bias} = 1.010 V, $t_{scanning}$ = 300 s, P_{start}= 2.185 mW and P_{finish}= 2.211 mW)

Figure S13. Certification results of flexible perovskite solar cells by the National Institute of Metrology, China (NIM, China).

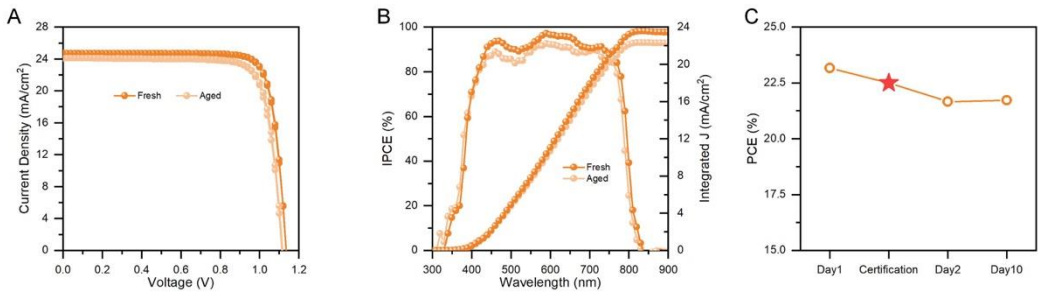

Figure S14. Performance of the unencapsulated fresh and aged MS-FPSC before and after certification. (A) *J-V* curves and (B) IPCE spectra of the unencapsulated fresh and aged flexible device. (C) PCE change of the certified MS-FPSC before and after certification. The day before certification is designated as Day 1. The take-out process led to a decline in the device performance, which can also be revealed in the current density, while it maintained the efficiency after storage in the dry box in our lab.

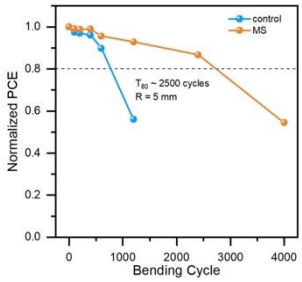

Figure S15. Normalized PCEs of control and MS-FPSCs after different bending cycles (bending radius = 5 mm, ~30% RH, ~ 25 °C).

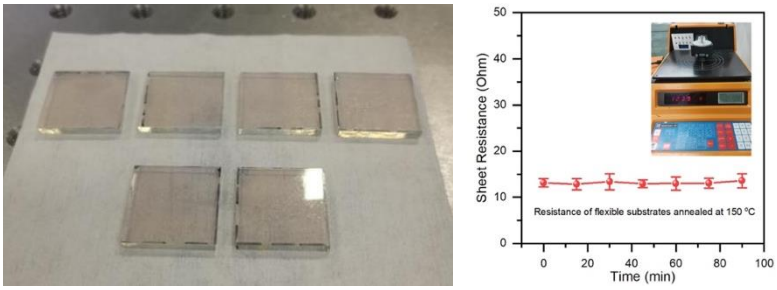

Figure S16. Images of flexible substrates after thermal annealing at 150 °C and the sheet resistance recorded during the annealing process. Carefully attached flexible substrates showed no deformation after the annealing process, and the sheet resistance remained normal.

Table S3. Extracted diffraction angle and FWHM data in Figure 3C, 3D.

Sample	2θ/°	FWHM/°	θ/rad	FWHM/rad	$4\sin\theta$	$\beta_T \cos\theta$
control	13.959	0.145	0.12182	0.00253	0.48606	0.00251
	19.82	0.164	0.17296	0.00286	0.6884	0.00282
	24.339	0.166	0.2124	0.0029	0.84322	0.00283
	28.121	0.149	0.2454	0.0026	0.97179	0.00252
	31.56	0.16	0.27541	0.00279	1.08778	0.00269
	40.281	0.204	0.35152	0.00356	1.37729	0.00334
	42.82	0.247	0.37367	0.00431	1.46016	0.00401
MS	13.999	0.142	0.12216	0.00248	0.48744	0.00246
	19.84	0.169	0.17314	0.00295	0.68909	0.00291
	24.36	0.146	0.21258	0.00255	0.84393	0.00249
	28.162	0.149	0.24576	0.0026	0.97317	0.00252
	31.581	0.15	0.2756	0.00262	1.08848	0.00252
	40.281	0.161	0.35152	0.00281	1.37729	0.00264
	42.84	0.2	0.37385	0.00349	1.46081	0.00325

Table S4. Extracted diffraction angle and FWHM data in Figure S9.

Sample	2θ/°	FWHM/°	θ/rad	FWHM/rad	$4\sin\theta$	$\beta_T \cos\theta$
control	14.06	0.153	0.1227	0.00267	0.48956	0.00265
	19.917	0.127	0.17381	0.00222	0.69174	0.00218
	24.4	0.187	0.21293	0.00326	0.8453	0.00319
	31.659	0.15	0.27628	0.00262	1.0911	0.00252
	34.781	0.276	0.30352	0.00482	1.19553	0.0046
MS	14.018	0.144	0.12233	0.00251	0.4881	0.00249
	19.861	0.1	0.17332	0.00175	0.68981	0.00172
	24.344	0.172	0.21244	0.003	0.84339	0.00293
	31.636	0.159	0.27608	0.00278	1.09033	0.00267
	34.701	0.158	0.30282	0.00276	1.19287	0.00263

Table S5. FWHM and estimated crystalline sizes of control and MS-perovskite films.

Sample	FWHM at (100)/°	Estimated Crystalline Sizes (nm)
control	0.145	55.2
MS	0.142	56.3

Table S6. Absorption energy of succinate anions on the $FAPbI_3$ surface.

	E_{abs}	$E_{MS+FAPbI_3}$	E_{MS}	E_{FAPbI_3}
FAI-terminated	-4.86	-2543.11	-73.64	-2464.62
PbI_2-terminated	-4.16	-2190.96	-73.61	-2113.19

References

1. Kaltenbrunner, M., Adam, G., Glowacki, E.D., et al. (2015). Flexible high power-per-weight perovskite solar cells with chromium oxide-metal contacts for improved stability in air. Nat Mater ***14***, 1032-1039.

2. Bu, T., Li, J., Li, H., et al. (2021). Lead halide-templated crystallization of methylamine-free perovskite for efficient photovoltaic modules. Science ***372***, 1327-1332.

3. Li, M., Zhou, J., Tan, L., et al. (2022). Brominated PEAI as multi-functional passivator for high-efficiency perovskite solar cell. Energy & Environ. Mater. eem2.12360.

4. Kresse, G., and Joubert, D. (1999). From ultrasoft pseudopotentials to the projector augmented-wave method. Phys. Rev. B ***59***, 1758-1775.

5. Perdew, J.P., Burke, K., and Ernzerhof, M. (1996). Generalized gradient approximation made simple. Phys. Rev. Lett. ***77***, 3865-3868.

6. Blöchl, P.E. (1994). Projector augmented-wave method. Phys. Rev. B ***50***, 17953-17979.

7. Grimme, S., Antony, J., Ehrlich, S., and Krieg, H. (2010). A consistent and accurate ab initio parametrization of density functional dispersion correction (DFT-D) for the 94 elements H-Pu. J. Chem. Phys. ***132***, 154104.